



# Effect of Heat Treatment on the Microstructure and Wear Properties of Al–Zn–Mg–Cu/In-Situ Al–9Si–SiCp/Pure Al Composite by Powder Metallurgy

Byung Chul Yu<sup>1</sup> · Ki-Chang Bae<sup>1</sup> · Je Ki Jung<sup>1</sup> · Yong-Hwan Kim<sup>2</sup> · Yong Ho Park<sup>1</sup>

Received: 30 June 2017 / Accepted: 16 August 2017 / Published online: 8 March 2018  
© The Korean Institute of Metals and Materials 2018

## Abstract

This study examined the effects of heat treatment on the microstructure and wear properties of Al–Zn–Mg–Cu/in-situ Al–9Si–SiCp/pure Al composites. Pure Al powder was used to increase densification but it resulted in heterogeneous precipitation as well as differences in hardness among the grains. Heat treatment was conducted to solve this problem. The heat treatment process consisted of three stages: solution treatment, quenching, and aging treatment. After the solution treatment, the main dissolved phases were  $\eta'$ (Mg<sub>4</sub>Zn<sub>7</sub>),  $\eta$ (MgZn<sub>2</sub>), and Al<sub>2</sub>Cu phase. An aging treatment was conducted over the temperature range, 100–240 °C, for various times. The GP zone and  $\eta'$ (Mg<sub>4</sub>Zn<sub>7</sub>) phase precipitated at a low aging temperature of 100–160 °C, whereas the  $\eta$ (MgZn<sub>2</sub>) phase precipitated at a high aging temperature of 200–240 °C. The hardness of the sample aged at 100–160 °C was higher than that aged at 200–240 °C. The wear test was conducted under various linear speeds with a load of 100 N. The aged composite showed a lower wear rate than that of the as-sintered composite under all conditions. As the linear speed was increased to 1.0 m/s, the predominant wear behavior changed from abrasive to adhesive wear in all composites.

**Keywords** Composites · Sintering · Wear · Scanning electron microscopy (SEM) · Heat treatment

## 1 Introduction

Recently, lightweight materials have attracted considerable attention in the automotive industry because of the ongoing demand to increase fuel efficiency. Therefore, ferrous materials are being replaced with aluminum alloys. A range of aluminum alloys are used in many fields according to the purpose. Among them, Al–Zn–Mg–Cu alloys, have attracted attention in the automotive industries because of their high strength to weight ratio and good wear resistance. Al–Zn–Mg–Cu alloy is strengthened by precipitation strengthening. A solution and aging treatment is an important process for improving the strength by controlling the

precipitation reaction. The following shows the most common precipitation sequence [1–5]:

Supersaturated solid solution → Guinier–Preston zone  
(GP zone) → metastable phase  $\eta'$ (Mg<sub>4</sub>Zn<sub>7</sub>)  
→ equilibrium phase  $\eta$ (MgZn<sub>2</sub>).

Al–Zn–Mg–Cu alloys are used in automotive transmission components, such as pistons, clutches, and sprockets, which require high strength and wear resistance. The strength and wear resistance of the Al–Zn–Mg–Cu alloys can be increased by adding ceramic reinforcements, such as silicon carbide and titanium carbide. Aluminum alloys that contain ceramic reinforcements are called aluminum matrix composites (AMCs) [6–8]. The powder metallurgy (P/M) route for manufacturing AMCs offers some advantages over other manufacturing processes. The P/M requires a low manufacturing temperature to avoid interfacial reactions and minimize the undesirable reactions between the matrix and reinforcement [9, 10]. In addition, the near-net shape qualities of P/M processing make it quite competitive with other manufacturing processes [11, 12].

✉ Yong Ho Park  
yhpark@pusan.ac.kr

<sup>1</sup> Department of Materials Science and Engineering, Pusan National University, Pusan 46241, Republic of Korea

<sup>2</sup> Graduate Institute of Ferrous Technology, Pohang University of Science and Technology, Pohang 37673, Republic of Korea

Despite the advantages, it is difficult to distribute reinforcement particles uniformly by powder metallurgy due to the low wettability between the aluminum and ceramic. Ceramic reinforcement particles segregate at the grain boundaries [8, 13, 14]. Segregation at the grain boundaries causes deterioration in the mechanical properties. Several methods to prevent the segregation of particles at the grain boundaries have been investigated; the use of the in-situ powder is one of them. In-situ powder contains the ceramic reinforcements in their grains that restrict segregation at the grain boundaries. Therefore, the ceramic reinforcements can avoid segregation after sintering.

Some studies have attempted to fabricate AMCs with in-situ powder due to the advantage of in-situ powder [15–17]. Among these studies, Lee fabricated Al–Zn–Mg–Cu matrix composites containing in-situ Al–9Si–SiCp powder to examine the effects of the in-situ powder on the wear behavior [15]. This study used Al–9Si alloy and pure Al powder to increase the sinterability by acting as a binder [17]. On the other hand, non-homogeneous precipitation that was induced by pure Al powder deteriorated the hardness and wear resistance. Despite this, few studies have attempted to solve this problem. The Al–Zn–Mg–Cu matrix composite could control precipitation by heat treatment. Therefore, in this study, heat treatment was conducted to control the distribution of precipitation and increase the hardness and wear resistance in the composite by changing the heat treatment conditions.

## 2 Experimental Procedures

### 2.1 Fabricating the Powders and Composites

A commercially available Al–Zn–Mg–Cu alloy powder (ECKA 431, ECKA Granules, Germany) and in-situ Al–9Si–SiCp composite powders were used for the study. The in-situ Al–9Si–SiCp composite powder was produced using a gas atomizer with 80% N<sub>2</sub> and 20% O<sub>2</sub> gas under a dynamic pressure of 2 MPa. SiC particles (20 vol%), 10–20 μm in size, were added to the molten Al–9Si alloy at 900 °C prior to gas atomization. Table 1 lists the chemical composition of each powder and Fig. 1 shows a cross-section of each powder. Each powder was analyzed by energy dispersive X-ray spectroscopy (EDS), as shown in Table 2. This indicates that the Alumix 431 powder consists of Al–Zn–Mg–Cu powder and pure Al powder, and a SiC particle was located in the Al–9Si powder successfully after in-situ processing. Alumix 431 and in-situ Al–9Si–SiCp powder were mixed (Alumix 431: Al–9Si–SiCp = 95:5 wt%) using a turbulent mixer at 45 rpm for 24 h. Hot

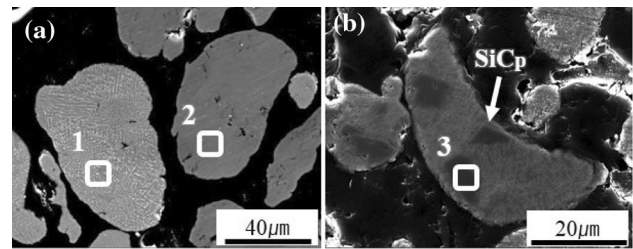


**Fig. 1** Cross-section of **a** Alumix 431 and **b** Al–9Si–SiCp composite powder

press sintering was then conducted with a uniaxial pressure of 70 MPa at 610 °C for 30 min [15]. The process was carried out under isothermal heat treatment conditions in a nitrogen atmosphere [18]. The sintered specimens were cooled in a hot press chamber.

### 2.2 Heat Treatments

To examine the effects of heat treatment on the composites, the composites were heat treated in a horizontal tube furnace. Heat treatment consisted of three stages: solution treatment, quenching, and aging treatment. Differential scanning calorimetry (DSC) was used to identify the temperature range of the solution and aging treatment. The composite was heated to 480 and 510 °C for several hours and quenched in water to obtain a supersaturated solid solution. The composite was then heated to precipitate the GP zone,  $\eta'$ (Mg<sub>4</sub>Zn<sub>7</sub>) and  $\eta$ (MgZn<sub>2</sub>) phase, under various temperatures (100–240 °C) and times (6–28 h). In this study, A.S.C. means the composite sintered at 610 °C for 30 min; S.T.C. means the composite solution treated at 510 °C for 1 h; and A.C. means the composite aging treated at 140 °C for 24 h after the solution treatment.

### 2.3 Microstructural and Heat Analysis

The microstructure of the composite was observed by field emission scanning electron microscopy (FE-SEM) with EDS. The phase constituents of the composites was analyzed by X-ray diffraction (XRD) using CuK $\alpha$  radiation. In addition, the thermal conductivity and thermal diffusivity of each composite were measured using a laser flash (LFA 467, NETZSCCH).

**Table 1** Chemical composition of each powder

wt%	Al	Zn	Mg	Cu	Si	SiC
Alumix 431	Bal.	5.9	2.5	1.7	–	–
Al–9Si–SiC <sub>p</sub>	Bal.	–	0.5	0.2	9	20 vol%

**Table 2** EDS analysis of each powder in Fig. 1

wt%	Al	Zn	Mg	Cu	Si	C
No. 1	83.11	10.21	04.06	02.62	–	–
No. 2	99.28	0.16	0.38	0.18	–	–
No. 3	01.26	–	–	–	81.10	17.64

## 2.4 Mechanical Properties

The hardness of the composites was measured using a micro Vicker's hardness tester with a load of 2.942 N. The wear test was carried out using a ball-on disc type tester. The material of the counter ball was SUJ2, which had a chemical composition of Fe–0.95C–0.15Si–0.2Mn–1.3Cr. The test was conducted under various linear speeds (0.1, 0.5, and 1.0 m/s) and an applied load of 100 N. The total sliding distance was fixed to 500 m and the test was performed in air at room temperature. The wear rate was calculated by the weight loss and true density of each composite. In addition, the wear track, cross-section, and debris were examined by SEM equipped with EDS. A K-type thermocouple was used to measure the friction temperature. A thermocouple was inserted into a small hole made at the middle of the specimen.

## 3 Results and Discussion

Figure 2 shows the microstructure and EDS data of the as-sintered composite. The microstructure can be divided into three types: Al–Zn–Mg–Cu, pure Al, and Al–9Si–SiCp areas, as shown in Fig. 2a. These areas were derived from the three types of powders used to fabricate the composite: Al–Zn–Mg–Cu powder, pure Al powder, and Al–9Si–SiCp powder.

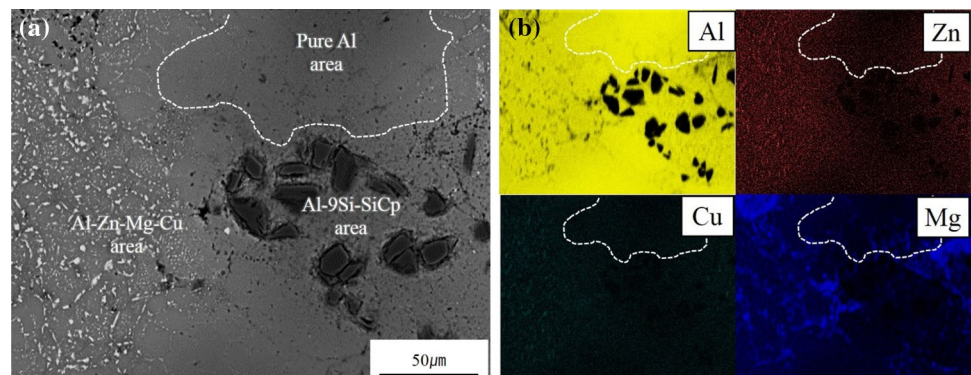
Al–Zn powder did not show a good sintering response because zinc is a poor sintering aid [19]. Therefore, pure Al powder was used to increase the extent of densification and sinterability during sintering. The pure Al powder has high plastic deformability and can be deformed easily by an

applied pressure. This contributes to binding and filling up of the space between the powders and improves densification during hot press sintering [16, 20]. The microstructure also shows that the SiC particles of the Al–9Si–SiCp area were distributed uniformly without segregation at the grain boundary by adding the in-situ powder.

In addition, the bright fine phase was observed in the Al–Zn–Mg–Cu area but no phase was found in the pure Al area, as shown in the Al–Zn–Mg–Cu and pure Al area of Fig. 2a. Figure 2b presents the EDS result of the as-sintered composite. Alloying elements, such as Zn, Mg, and Cu were detected in the bright fine phase of the Al–Zn–Mg–Cu area. In contrast, the alloying elements were rarely detected in the pure Al area.

Figure 3 shows XRD patterns of the as-sintered composite. This shows that  $\alpha$ -Al, hexagonal  $\eta$ (MgZn<sub>2</sub>: ICSD collection code: 108587), monoclinic  $\eta'$ (Mg<sub>4</sub>Zn<sub>7</sub>: ICSD collection code: 104899), tetragonal Al<sub>2</sub>Cu (ICSD collection code: 172800), and cubic SiC (ICSD collection code: 164973) exist in the as-sintered composite.

Figure 4 presents the DSC data of the as-sintered and solution-treated composite. Point A of the DSC curve of the as-sintered composite revealed an endothermic peak between 500 and 520 °C. Points B and C of the DSC curve of the solution-treated composite showed endothermic and exothermic peaks. In general, the endothermic peak represents the dissolution reaction, whereas the exothermic peak represents the precipitation reaction. A previous study showed that the melting temperature associated with a  $\eta$  phase in the Al–Zn–Mg–Cu alloy was approximately 500 °C [21]. Point A is related to dissolution of the  $\eta$  phase. Therefore, the solution treatment of the as-sintered composite was conducted at 480 and 510 °C for various times. In addition,

**Fig. 2** a Microstructure and b EDS result of the as-sintered composite

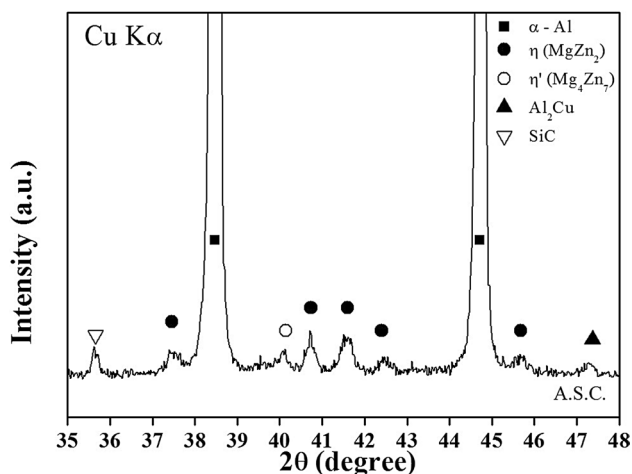


Fig. 3 XRD pattern of the as-sintered composite

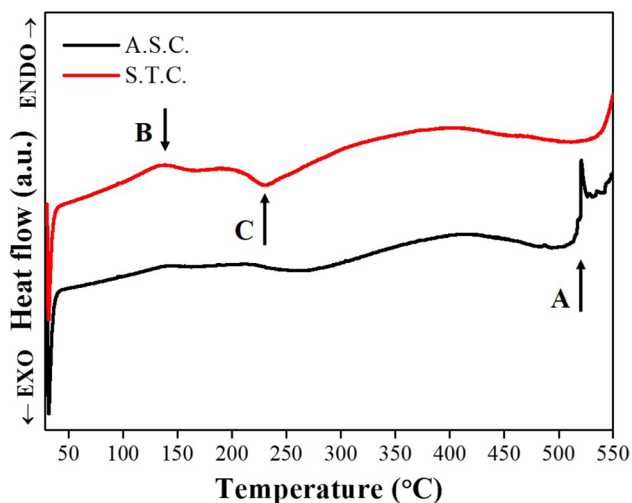


Fig. 4 DSC curve of the as-sintered and solution-treated composite

the Al–Zn–Mg–Cu alloy has the following precipitation sequence after the solution treatment. The Al–Zn–Mg–Cu alloy becomes a supersaturated solution with a GP zone. The GP zone is coherent with the aluminum matrix. With increasing time or temperature, a metastable  $\eta'$ (Mg<sub>4</sub>Zn<sub>7</sub>) phase developed that was semi-coherent with the matrix and had a monoclinic unit cell. With increasing time or temperature, the  $\eta'$ (Mg<sub>4</sub>Zn<sub>7</sub>) phase transformed to an incoherent equilibrium  $\eta$ (MgZn<sub>2</sub>) phase, which has a hexagonal unit cell. The GP zone was reported to dissolve at 150 °C and the  $\eta'$ (Mg<sub>4</sub>Zn<sub>7</sub>) and  $\eta$ (MgZn<sub>2</sub>) phase formed at 200 °C [12]. Therefore, in the DSC curve of the solution-treated composite, point B between 130 and 150 °C represents the dissolution of the GP zone and point C between 220 and 240 °C represents the formation of the  $\eta$ (MgZn<sub>2</sub>) phase. To control precipitation through an aging treatment, the range

of aging temperatures was determined to be 100 to 240 °C based on the DSC results.

The dissolution and formation reaction, such as points B and C, were not observed on the DSC curve of the as-sintered composite, as shown in Fig. 4. The as-sintered composite, which was cooled slowly in the furnace, contained a considerable fraction of equilibrium  $\eta$ (MgZn<sub>2</sub>) phase and metastable  $\eta'$ (Mg<sub>4</sub>Zn<sub>7</sub>) phase. Because the  $\eta$ (MgZn<sub>2</sub>) phase had already formed in the as-sintered composite, the formation reaction of the  $\eta$ (MgZn<sub>2</sub>) and  $\eta'$ (Mg<sub>4</sub>Zn<sub>7</sub>) phase and the dissolution of the GP zone were not observed in the as-sintered composite.

Figure 5 shows XRD patterns of the solution-treated composite under various solution treatment conditions: 480 and 510 °C for 1, 2, and 3 h. This suggests that the peak of  $\eta$ (MgZn<sub>2</sub>) and Al<sub>2</sub>Cu phase disappeared under all solution treatment conditions except for the condition of 480 °C for 1 h. On the other hand, the peak of the  $\eta'$ (Mg<sub>4</sub>Zn<sub>7</sub>) phase was detected by XRD. Some of the GP zone, which had been formed by quenching, were transformed to the  $\eta'$ (Mg<sub>4</sub>Zn<sub>7</sub>) phase with increasing time. This is why the  $\eta'$ (Mg<sub>4</sub>Zn<sub>7</sub>) phase was detected despite the solution treatment. In addition, the peak of the GP zone was not detected by XRD because it is fine and coherent with the matrix [12].

Figure 6 shows (a) the microstructure and (b) EDS data of the solution-treated composite under 510 °C for 1 h. EDS mapping was conducted at the areas showing both Al–Zn–Mg–Cu and pure Al. At the Al–Zn–Mg–Cu area, the bright fine phase was almost dissolved as a result of the solution treatment, as shown in Fig. 6a. Furthermore, Zn and Mg were detected in the pure Al area of the solution-treated composite compared to the pure Al area of the as-sintered composite, as shown in Fig. 6b. This can be explained by

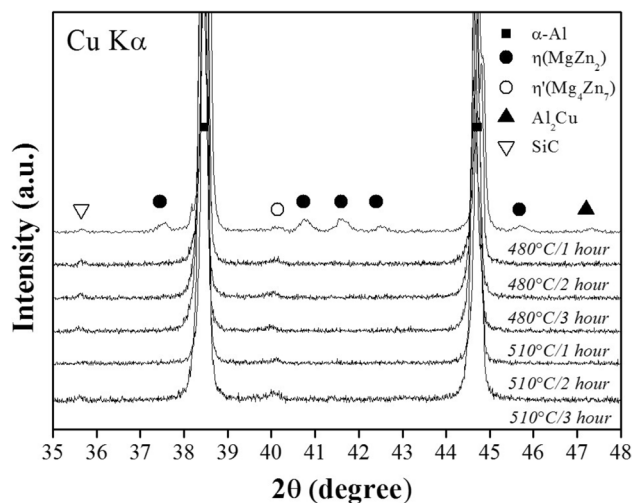
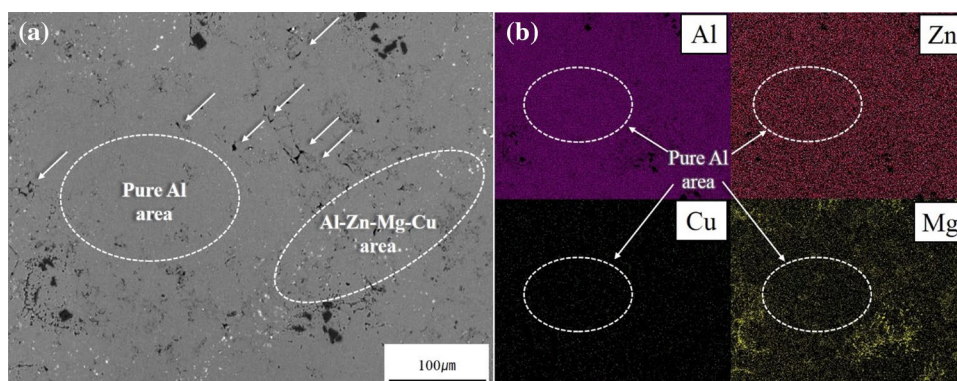


Fig. 5 XRD pattern analysis of the solution-treated composite under various conditions



**Fig. 6** **a** Microstructure and **b** EDS result of the solution-treated composite



atomic diffusion. During the solution treatment, the diffusion of Zn and Mg occurred from the Al–Zn–Mg–Cu area to the pure Al area at high temperature, which provides the driving force for diffusion.

In addition, the SEM microstructure show that the pores (arrowed) were created along the grain boundaries after solution treatment. As shown in Table 4, the relative density of the composite decreased significantly after the solution treatment. The composite was fabricated through powder metallurgy. The composite was cooled slowly in the furnace after sintering processing. Precipitation of the phase is expected to occur at the grain boundaries and free surfaces, including the internal pore surfaces. This leads to a considerable increase in the relative density of the composite [22]. When the composite was heat treated for the solution treatment, the phase formed at grain boundaries and free surfaces were dissolved with the concomitant formation of pores. This might lead to a decrease in the relative density of the composite.

Before the solution treatment, there was difference in hardness between the Al–Zn–Mg–Cu and pure Al areas: 252.5 HV and 171.4 HV, respectively, as shown in Table 3. After the solution treatment, however, not only the hardness of the composite increase but also the difference in hardness between Al–Zn–Mg–Cu and pure Al area almost disappeared. At a solution treatment temperature of 480 °C, the hardness of the composite began to decrease after more than 3 h. At a solution treatment temperature of 510 °C, the hardness began to decrease after more than 2 h. In contrast, the difference in hardness continued to decrease with increasing solution treatment time. In addition, the difference in the hardness at 510 °C is lower than that at 480 °C. Therefore, it is considered that the solution treatment condition of 510 °C for 1 h is the better condition. Overall, the hardness of the Al–Zn–Mg–Cu and pure Al areas reached up to 285.7 and 272.6 HV, respectively at a solution treatment temperature 510 °C for 1 h. Furthermore, the difference in hardness decreased from 81.1 to 13.1 HV.

Figure 7 presents XRD patterns of the aged composite at various temperatures (100, 160, 200, and 240 °C) for 24 h

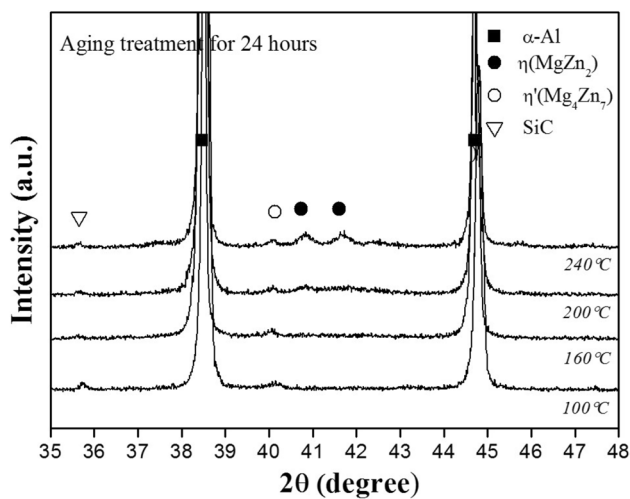
**Table 3** Micro Vicker's hardness of the solution-treated composite according to the solution treatment conditions: (a) 480 °C for 1 h, (b) 480 °C for 2 h, (c) 480 °C for 3 h, (d) 480 °C for 4 h, (e) 510 °C for 1 h, (f) 510 °C for 2 h, (g) 510 °C for 3 h, (h) 510 °C for 4 h

Specimen	Hardness of Al–Zn–Mg–Cu area (HV)	Hardness of pure Al area (HV)	Differences in hardness (HV)
A.S.C.	252.5	171.4	81.1
(a)	283.7	208.9	74.8
(b)	288.0	248.4	39.6
(c)	287.8	251.3	36.5
(d)	265.6	238.5	27.1
(e)	285.7	272.6	13.1
(f)	285.2	275.1	11.4
(g)	273.2	268	5.2
(h)	244.9	241.7	3.2

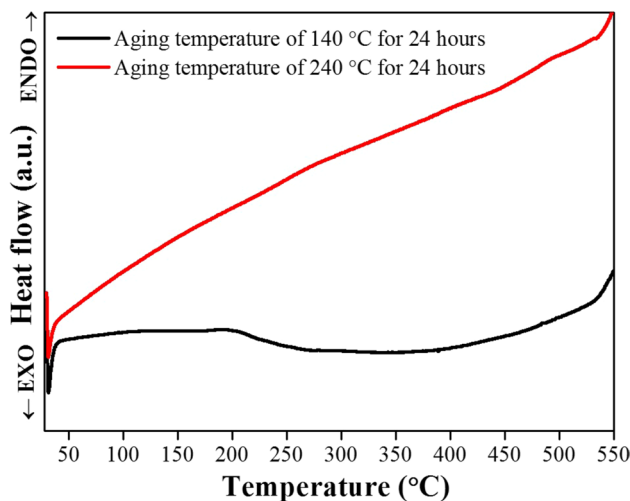
after a solution treatment at 510 °C for 1 h. The peak of the  $\eta'$ (Mg<sub>4</sub>Zn<sub>7</sub>) and  $\eta$ (MgZn<sub>2</sub>) phase was detected after an aging treatment at 200 and 240 °C for 24 h, while only the peaks for the  $\eta'$ (Mg<sub>4</sub>Zn<sub>7</sub>) phase were detected under after the aging treatment at 100 and 160 °C for 24 h.

Figure 8 presents the DSC data of the aged composite at 140 and 240 °C for 24 h. The DSC curve of the aged composite at 140 °C for 24 h revealed the dissolution reaction of the GP zone and the precipitation reaction of the  $\eta'$ (Mg<sub>4</sub>Zn<sub>7</sub>) and  $\eta$ (MgZn<sub>2</sub>) phase. This means that the composite heat treated at 140 °C for 24 h consists of the GP zone. On the other hand, no reaction occurred at 240 °C for 24 h because this composite already consists of the  $\eta'$ (Mg<sub>4</sub>Zn<sub>7</sub>) and  $\eta$ (MgZn<sub>2</sub>) phase. Therefore, according to the results of XRD and DSC analysis, the composite consists of a GP zone and  $\eta'$ (Mg<sub>4</sub>Zn<sub>7</sub>) phase after the aging treatment at 100–160 °C. In addition, after aging at 200 and 240 °C, the composite consists of a  $\eta'$ (Mg<sub>4</sub>Zn<sub>7</sub>) and  $\eta$ (MgZn<sub>2</sub>) phase.

Figure 9 shows the hardness of the aged composite at various aging temperatures and times. As mentioned above, the difference in hardness between the Al–Zn–Mg–Cu and pure Al areas of the solution-treated composite almost

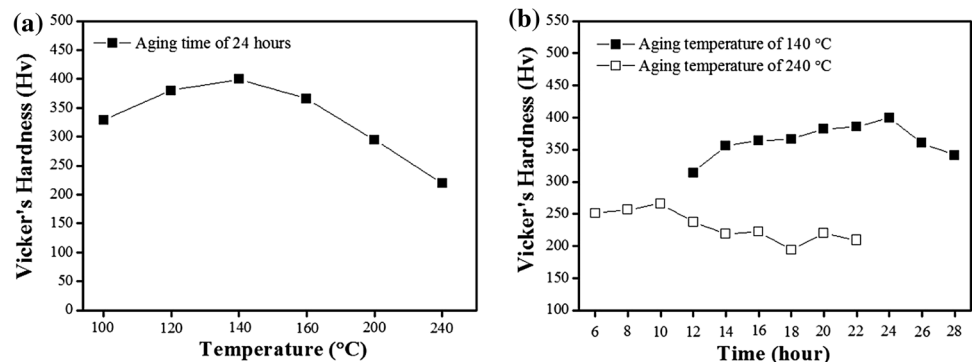


**Fig. 7** XRD pattern of solution-treated and aged composite under various conditions



**Fig. 8** DSC curve of the aged composite at 140 and 240 °C for 24 h

**Fig. 9** Micro Vicker's hardness of the aged composite according to the aging treatment conditions: **a** various temperatures for 24 h, **b** various times at 140 and 240 °C



disappeared. The hardness of the Al–Zn–Mg–Cu area in the aged composite was similar to that of the pure Al area. The hardness of the composite aged at various temperatures for 24 h was measured, as shown in Fig. 9a. The composite aged at low temperatures (100–160 °C) showed higher hardness than that at high temperatures (200–240 °C). In addition, Fig. 9b shows the hardness of the aged composite for various aging times at 140 and 240 °C. At an aging treatment temperature of 140 °C, the hardness of the composite continued to increase with increasing holding time. After more than 24 h, the hardness began to decrease. Similarly, at an aging treatment temperature of 240 °C, the hardness of the composite continued to increase with increasing holding time. On the other hand, the hardness began to decrease after more than 10 h. Overall, the composite aged at 140 °C showed higher hardness than at 240 °C. This suggests that the GP zone and  $\eta'$ (Mg<sub>4</sub>Zn<sub>7</sub>) phase contribute more to age hardening than the  $\eta'$ (Mg<sub>4</sub>Zn<sub>7</sub>) and  $\eta$ (MgZn<sub>2</sub>) phases.

Figure 10 shows (a) the wear rate and (b) friction temperature of each composite at a linear speed of 0.1, 0.5, and 1.0 m/s with an applied load of 100 N. The solution-treated composite was heat treated at 510 °C for 1 h. The aged composite was heat treated at 140 °C for 24 h after the solution treatment at 510 °C for 1 h. The wear rate of the aged composite was lower than that of the as-sintered and solution-treated composite under all wear conditions. At a linear speed from 0.1 to 0.5 m/s, the change in wear rate was insignificant in all composites. When the linear speed was increased from 0.5 to 1.0 m/s, the wear rate increased significantly in the as-sintered composite. On the other hand, at a linear speed from 0.5 to 1.0 m/s, the aged composite showed relatively little change in wear rate. The wear resistance of the aged composite increased due to the increase in hardness of the aged composite by aging hardening. In contrast, the wear resistance of the solution treated composite decreased despite increasing in hardness.

The friction temperature of each composite increased linearly with increasing linear speed. In particular, the friction temperature of the solution-treated composite was higher than that of the other composite under all wear conditions.

**Fig. 10** **a** Wear rate and **b** friction temperature of each composite under various wear conditions

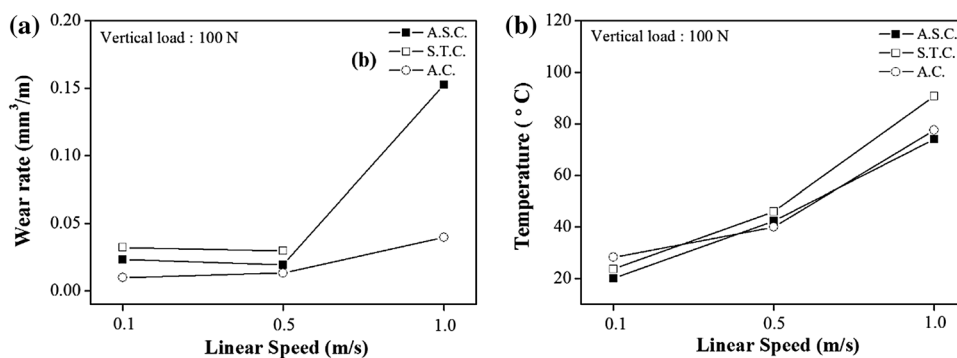


**Table 4** Properties of the as-sintered, solution-treated, and aged composite

Specimen	Relative density (%)	Thermal diffusivity (mm²/S)	Thermal conductivity [W/(m*K)]
A.S.C.	98.5	53.9	147.9
S.T.C.	95.8	45.0	120.1
A.C.	95.8	51.3	137.0

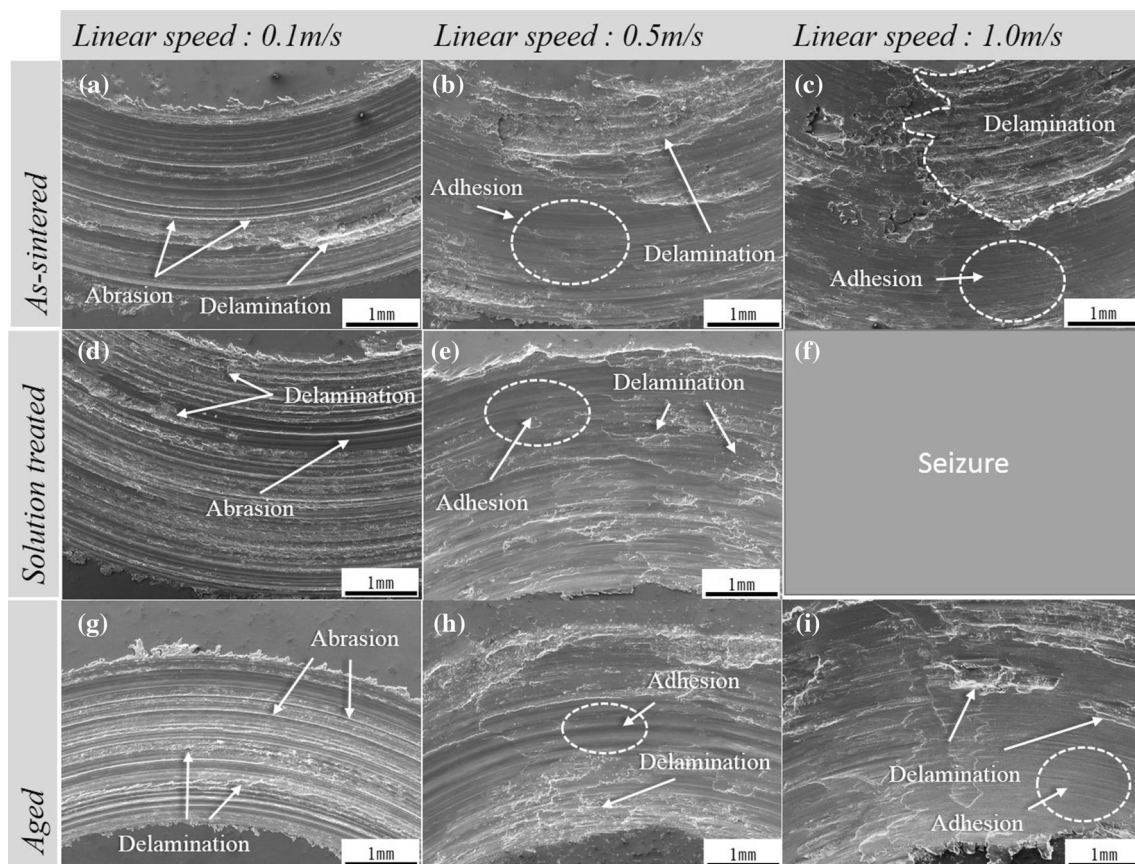
The relative density, the thermal diffusivity and the thermal conductivity of the solution-treated composite were lower than that of the as-sintered composite, as shown in Table 4. As mentioned above, many pores formed along the grain boundaries led to a decrease in the relative density after the solution treatment. These pores could act as crack initiation points during the wear test. In addition, after the solution treatment, the lattice of the matrix was distorted by dissolved atoms, such as Zn and Mg. These atoms in the matrix act as obstacles to electrons, which is the principal carrier of heat energy, and disturb heat transfer [23]. This leads to a decrease in thermal conductivity and an increase in friction temperature in the composite. An elevation in temperature due to the friction temperature softened the composite, which resulted in an increased wear rate [24]. These are the reasons why the solution treated composite has low wear resistance.

Figure 11 shows the wear track of each composite under a linear speed of 0.1, 0.5, and 1.0 m/s with an applied load of 100 N. Similar wear behavior was observed in all composites according to the linear speed. At a linear speed of 0.1 m/s, abrasive wear is the major wear behavior in all composites. Abrasive wear generates a groove pattern and small delamination on the wear track, as shown in Fig. 11a, d, g. According to the increased linear speed from 0.1 to 0.5 m/s, the groove pattern almost disappeared and some adhesion and delamination started to occur on the wear track, as shown in Fig. 11b, e, h. According to the increased linear speed from 0.5 to 1.0 m/s, adhesive wear was predominantly observed and large delamination occurred, as shown in Fig. 11c, i. As

shown in Fig. 10a, a substantial increase in wear rate was observed when the linear speed was increased from 0.5 to 1.0 m/s. Adhesive wear was accompanied by thermal plastic deformation and material loss, which caused an increase in wear rate [25]. Therefore, adhesive wear became the predominant wear behavior with increasing linear speed from 0.5 to 1.0 m/s and caused an increase in wear rate.

Figure 12 presents the wear cross-section of each composite under a linear speed of 0.1, 0.5, and 1.0 m/s with an applied load of 100 N and Table 5 lists the EDS data of the wear cross-section of the aged composite at a linear speed of 0.5 m/s. Voids and cracks were observed at the cross-section under all conditions, and were generated under the surface during the wear test. They then grew almost parallel to the surface and were removed from the surface. The removed material became wear debris [24]. In addition, the dark layer near the surface of the wear cross-section was observed at a linear speed of 0.5 m/s. EDS indicated that the dark layer contained a large amount of oxide and carbon compared to the under layer, as shown in Table 5. In general, as the friction temperature increases with increasing linear speed, the atoms of the counter materials are transferred to the surface of the composite and form an oxide layer during the wear test. The oxide layer, which develops during the wear test, protects the surface from the counter materials and minimizes the adhesive wear by preventing contact between the surface and counter materials [24]. The friction temperature increased linearly with increasing linear speed from 0.1 to 0.5 m/s. SUJ2, which contained carbon, was used as the counter material in this study. Therefore, the carbon in SUJ2 was transferred to the surface with increasing friction temperature during the wear test, which contributed to the development of an oxide layer containing carbon on the surface. The developed oxide layer protected the surface. Therefore, the change in wear rate was insignificant despite increasing the linear speed from 0.1 to 0.5 m/s. This oxide layer was not observed when the linear speed was increased from 0.5 to 1.0 m/s because the oxide layer was destroyed with increasing linear speed.





**Fig. 11** Wear track of each composite under various wear conditions

Figure 13 shows the wear debris of each composite at a linear speed of 0.1, 0.5, and 1.0 m/s with an applied load of 100 N. The debris consisted mainly of small blocky debris and some flake-like debris in all composites at a linear speed of 0.1 m/s. As the linear speed was increased from 0.1 to 1.0 m/s, the main debris transformed from small blocky to flake-like debris. In general, the small block debris is generated by abrasive wear, whereas the flake-like debris is generated mainly by adhesive wear. Adhesive wear is accompanied by thermal plastic deformation. Flake-like debris can be generated by plastic deformation. Hard asperities over a softer surface without cutting will produce ridges. These ridges can be flattened by further contact. The flattened material on the surface breaks off and becomes flat wear flakes [26]. The size of the debris of the aged composite was smaller than that of the other composite. In general, the size of the debris is small when the material has high hardness because crack propagation deep from the surface is difficult. This suggests that aging hardening has a positive impact on the wear resistance of the composite.

Overall, at a linear speed of 0.1 m/s, abrasive wear is the predominant behavior in all composites. The wear rate at a linear speed of 0.5 m/s showed a similar wear rate at a

linear speed of 0.1 m/s because an oxide layer was formed at all composites, which protects the surface and decreases the wear rate. According to the increasing linear speed up to 1.0 m/s, the wear behavior was changed from abrasive to adhesive wear and the wear rate increased rapidly except for the aged composite. The oxide layer was not observed in any of the composites. Therefore, the surface of the composite was not protected against the counter materials. At a linear speed of 1.0 m/s, only the aged composite, which consists of a GP zone and  $\eta'$ ( $\text{Mg}_4\text{Zn}_7$ ) phase, could endure the stress. In contrast, the solution-treated composite showed low wear resistance despite solid solution hardening.

## 4 Conclusions

An Al–Zn–Mg–Cu/in-situ Al–9Si–SiCp/pure Al composite was fabricated by hot press sintering. The effects of heat treatment in the composite were examined. The heat treatment consisted of three stages: solution treatment, quenching, and aging treatment. The solution and aging treatment were conducted under a range of temperatures and times.



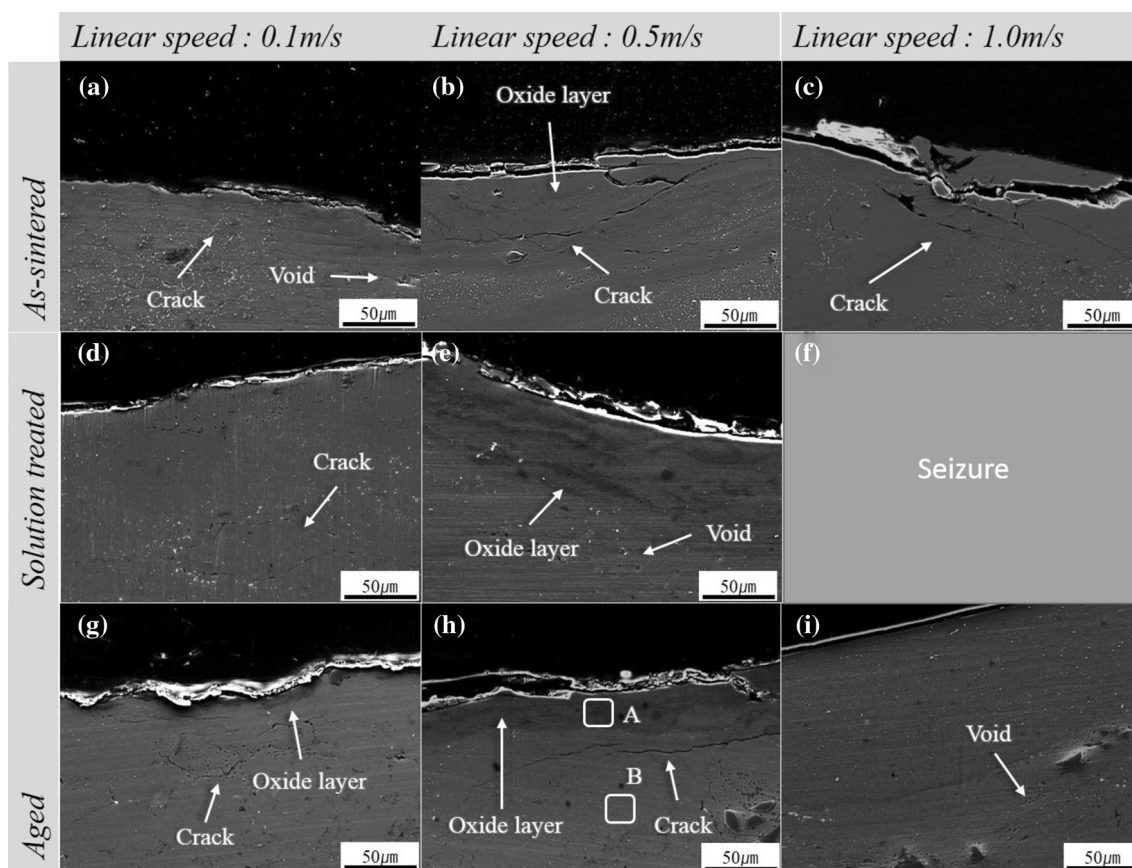


**Fig. 12** Wear cross-section of each composite under various wear conditions

**Table 5** EDS analysis of wear cross-section of the aged composite at a linear speed of 0.5 m/s

Point	Al	Zn	Mg	Cu	Si	C	O
No. A	73.06	1.88	2.57	–	2.09	11.16	09.16
No. B	94.67	02.47	02.03	–	–	–	00.83

1. After sintering, the microstructure consisted of three different areas. Alloying elements were not detected in the pure Al area, which caused a difference in hardness among the areas.
2. After the solution treatment, the main phase,  $\eta'$ (Mg<sub>4</sub>Zn<sub>7</sub>),  $\eta$ (MgZn<sub>2</sub>), and Al<sub>2</sub>Cu phase, dissolved in the composite and alloying elements were detected in all three areas. In addition, the difference in hardness among the areas almost disappeared. The optimized solution treatment was found to be 510 °C for 1 h according to the difference in hardness.
3. At an aging temperature of 100–160 °C, the composite consisted mainly of a GP zone and  $\eta'$ (Mg<sub>4</sub>Zn<sub>7</sub>) phase. At an aging temperature of 200–240 °C, the composite consisted
4. In all composites, the wear behavior changed from abrasive to adhesive wear with increasing linear speed from 0.1 to 1.0 m/s. The wear rate of the aged composite was lower than that of the as-sintered composite under all wear conditions. In particular, the wear rate of the as-sintered composite increased significantly when the linear speed was increased from 0.5 to 1.0 m/s. Especially, the solution-treated composite exhibited low wear resistance.

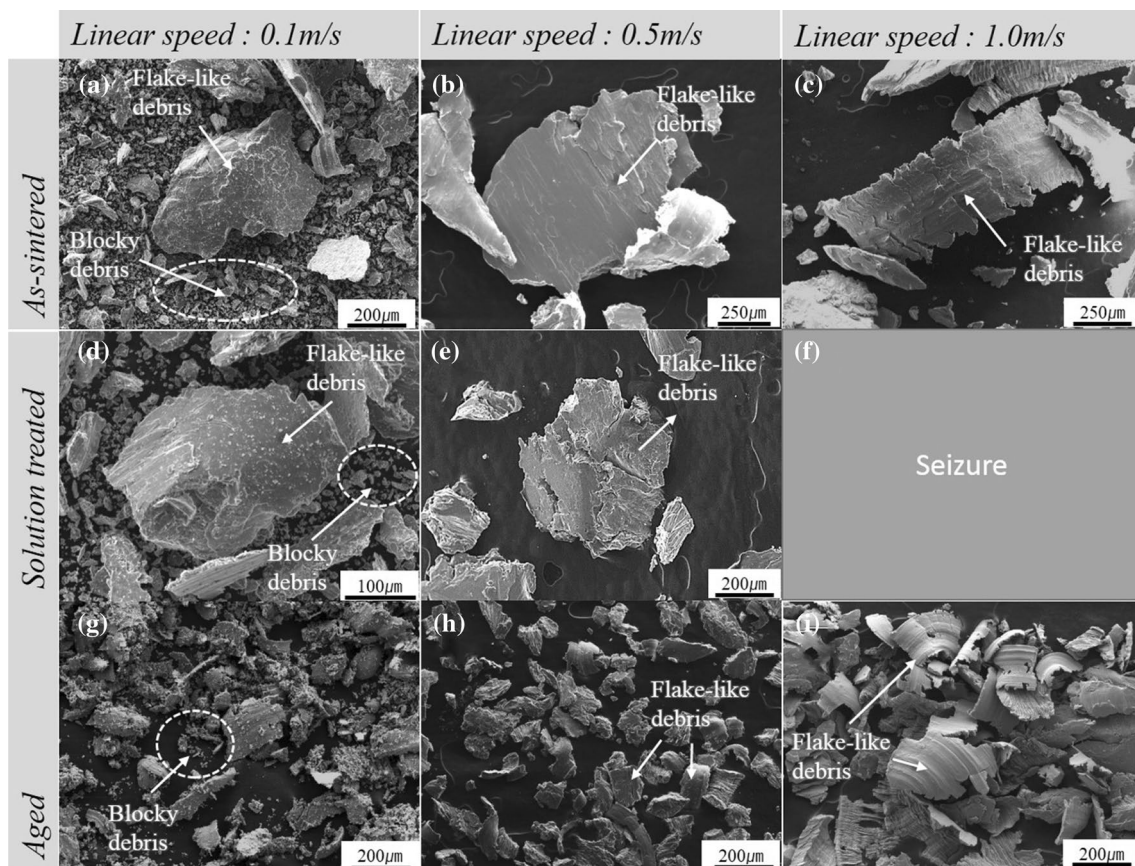


**Fig. 13** Wear debris of each composite under various wear conditions

**Acknowledgements** This work was supported by the National Research Council of Science & Technology (NST) grant by the Korea government (MSIT) (No. CRC-15-03-KIMM).

## References

- J.C. Werenskiold, A. Deschamps, Y. Bréchet, *Mater. Sci. Eng. A* **293**, 267–274 (2000)
- M. Chemingui, M. Khitouni, K. Jozwiak, G. Mesmacque, A. Kolsi, *Mater. Des.* **31**, 3134–3139 (2010)
- K.A. Ragab, M. Dellah, M. Bournane, Y. Sadaoui, *Int. J. Cast Met. Res.* **28**, 257–262 (2015)
- S.W. Kim, D.Y. Kim, W.G. Kim, K.D. Woo, *Mater. Sci. Eng. A* **304–306**, 721–726 (2001)
- K. Chen, H. Liu, Z. Zhang, S. Li, R.I. Todd, *J. Mater. Process. Technol.* **142**, 190–196 (2003)
- T.S. Srivatsan, I.A. Ibrahim, F.A. Mohamed, E.J. Lavernia, *J. Mater. Sci.* **26**, 5965–5978 (1991)
- A. Baradeswaran, A. Elaya, *Perumal. Compos. Part B Eng.* **56**, 464–471 (2014)
- G. B. Schaffer, *Mater. Forum*, 2004, pp. 65–74
- J.M. Torralba, C.E. da Costa, F. Velasco, *J. Mater. Process. Technol.* **133**, 203–206 (2003)
- B. Ogel, R. Gurbuz, *Mater. Sci. Eng. A* **301**, 213–220 (2001)
- S.S. Su, I.T.H. Chang, W.C.H. Kuo, *Mater. Chem. Phys.* **139**, 775–782 (2013)
- A.D.P. LaDelphi, H. Neubing, D.P. Bishop, *Mater. Sci. Eng. A* **520**, 105–113 (2009)
- A. Ahmed, A.J. Neely, K. Shankar, P. Nolan, S. Moricca, T. Eddowes, *Metall. Mater. Trans. A* **41**, 1582–1591 (2010)
- G. O'Donnell, L. Looney, *Mater. Sci. Eng. A* **303**, 292–301 (2001)
- E.S. Lee, J.-J. Oak, J. Bang, Y.H. Park, *J. Alloys Compd.* **689**, 145–152 (2016)
- J. Bang, J.-J. Oak, Y.H. Park, *J. Mater. Eng. Perform.* **25**, 102–115 (2016)
- M.L. Delgado, E.M. Ruiz-Navas, E. Gordo, J.M. Torralba, *J. Mater. Process. Technol.* **162–163**, 280–285 (2005)
- G.B. Schaffer, B.J. Hall, S.J. Bonner, S.H. Huo, T.B. Sercombe, *Acta Mater.* **54**, 131–138 (2006)
- G.B. Schaffer, T.B. Sercombe, R.N. Lumley, *Mater. Chem. Phys.* **67**, 85–91 (2001)
- I. Arribas, J.M. Martín, F. Castro, *Mater. Sci. Eng. A* **527**, 3949–3966 (2010)
- D.K. Xu, P.A. Rometsch, N. Birbilis, *Mater. Sci. Eng. A* **534**, 234–243 (2012)
- R.N. Lumley, G.B. Schaffer, *Scr. Mater.* **55**, 207–210 (2006)
- C. Wang, Z. Liu, S. Xiao, Y. Chen, *Mater. Sci. Technol.* **32**, 581–587 (2016)
- R.L. Deuis, C. Subramanian, J.M. Yellup, *Compos. Sci. Technol.* **57**, 415–435 (1997)
- M.A. Herbert, R. Maiti, R. Mitra, M. Chakraborty, *Wear* **265**, 1606–1618 (2008)
- B. Bhushan, *Modern Tribology Handbook, Two Volume Set* (CRC Press, Boca Raton, 2000)